AGU PUBLICATIONS

JGR

Journal of Geophysical Research: Oceans

RESEARCH ARTICLE

10.1002/2015JC011380

Special Section:
Physical Processes Responsible for Material Transport in the Gulf of Mexico for Oil Spill Applications

Effects of swell on transport and dispersion of oil plumes within the ocean mixed layer

Bicheng Chen[1], Di Yang[2], Charles Meneveau[3], and Marcelo Chamecki[1]

[1]Department of Meteorology, Pennsylvania State University, University Park, Pennsylvania, USA, [2]Department of Mechanical Engineering, University of Houston, Houston, Texas, USA, [3]Department of Mechanical Engineering, Johns Hopkins University, Baltimore, Maryland, USA

Abstract The transport in the ocean mixed layer (OML) of oil plumes originated from deepwater blowouts is studied using large eddy simulations. In particular, we focus on the effects of swell on the modulation of turbulence in the OML and its impact on oil transport. Results show that when the misalignment between the wind and the swell propagation is small, Langmuir cells develop and significantly enhance the vertical dilution of the oil plume. Conversely, when the misalignment is large, vertical dilution is suppressed when compared to the no-swell case. Due to the strong directional shear of the mean flow within the OML, plume depth significantly impacts mean transport direction. The size of oil droplets in the plume also plays an important role in vertical dilution and mean transport direction.

Key Points:
- Swell can enhance or suppress the vertical eddy diffusivity for oil, depending on swell-wind angle
- Vertical oil distribution significantly impacts the mean transport direction of oil plume
- Oil droplet size also plays an important role in vertical dilution and mean transport direction

Correspondence to:
M. Chamecki,
chamecki@psu.edu

Citation:
Chen, B., D. Yang, C. Meneveau, and M. Chamecki (2016), Effects of swell on transport and dispersion of oil plumes within the ocean mixed layer, *J. Geophys. Res. Oceans*, *121*, 3564–3578, doi:10.1002/2015JC011380.

Received 8 OCT 2015
Accepted 4 MAY 2016
Accepted article online 9 MAY 2016
Published online 27 MAY 2016

1. Introduction

Predicting transport, dilution, and fate of oil released from deepwater blowouts has become a topic of great interest after the Deepwater Horizon (DWH) oil spill in the Gulf of Mexico in 2010. Oil plumes from deepwater blowouts rise through different ocean layers, experiencing a large range of flow conditions. Once the oil reaches the uppermost ocean layer (the ocean mixed layer, OML), its transport is impacted by a number of physical processes including shear and buoyancy generated turbulence, surface gravity waves, Ekman transport and submeso-scale and meso-scale quasi-geostrophic flows. The interplay between all these processes impacts the characteristics of the surface oil plume and must be taken into account in predictions of oil spill evolution and in the development a contingency plans. The focus of this work is on the small-scale processes, such as shear turbulence and Langmuir circulations, which play an important role in the transport of oil but are not explicitly represented in regional and global ocean models [e.g., *Le Henaff et al*., 2012; *Huntley et al*., 2013].

The dynamics of the OML are, in large part, driven by the wind [*Phillips*, 1966; *Sullivan and McWilliams*, 2010]. The wind stress acting on the ocean surface drives a current that, in turn, leads to the production of shear turbulence. In addition, surface gravity waves interact with the mean surface ocean current, leading to the development of shallow counter-rotating vortex pairs called Langmuir cells [*Langmuir*, 1938]. Langmuir cells play an important direct role in upper ocean mixing [*Leibovich*, 1983]. In addition, these cells interact nonlinearly with shear generated turbulence, modulating turbulence intensities in a regime usually referred to as Langmuir turbulence [*McWilliams et al*., 1997].

The behavior of oil plumes in Langmuir turbulence has been recently studied using numerical modeling based on the large eddy simulation (LES) technique [*Yang et al*., 2014, 2015]. LES has been widely used in studies of Langmuir turbulence [e.g., *Skyllingstad and Denbo*, 1995; *McWilliams et al*., 1997; *Noh et al*., 2004] and it has been shown to produce results in good agreement with observations [e.g., *Kukulka et al*., 2009; *Scotti*, 2010]. LES results for oil dispersion have shown that the spatial patterns of the surface oil plume, as well as its vertical distribution within the OML, depend both on the size of the oil droplets and on the strength of the Langmuir circulations [*Yang et al*., 2014]. These effects can be represented by the drift-to-buoyancy ratio (*Db*), a dimensionless parameter based on the rise velocity of oil droplets and the magnitude of the Stokes drift velocity [*Yang et al*., 2014]. In addition, *Db* has been shown to be a useful parameter in describing the direction of transport and the lateral spread of the mean oil plume in the OML [*Yang et al*., 2015].

In all the aforementioned studies of oil transport in Langmuir turbulence, the wave field was assumed to be aligned with the mean wind. However, this is usually not the case in realistic conditions [*Hanley et al*., 2010]. In particular, swell waves are usually independent of the local wind field and can have considerable misalignment with the mean wind direction. Thus, in practice, the direction of the mean wind shear on the ocean surface and the direction of the wave propagation are often different. This misalignment has a profound effect on the strength and orientation of Langmuir cells and on the modulation of turbulence [*Van Roekel et al*., 2012; *McWilliams et al*., 2014]. The effects of swell on oil transport within the OML have not been explored and are the main focus of this work. The LES model developed by *Yang et al*. [2014, 2015] is used to explore the response of oil plumes with different droplet sizes to systematic increases in the misalignment between the mean wind stress and the swell wave. The LES model and the simulation setup used here are briefly described in section 2. Results from the LES are presented in section 3. Conclusions follow in section 4.

2. LES Model

2.1. Model Description

The LES model employed in this study is described in detail by *Yang et al*. [2015], and only a brief summary is presented here. We follow the typical approach to simulate Langmuir turbulence in the OML using LES (without explicitly resolving the waves) based on the filtered Craik-Leibovich equations [e.g., *McWilliams et al*., 1997; *Skyllingstad*, 2000; *Kukulka et al*., 2009; *Yang et al*., 2015]. More specifically, we solve

$$\frac{\partial \tilde{\mathbf{u}}}{\partial t}+\tilde{\mathbf{u}}\cdot\nabla\tilde{\mathbf{u}}=-\frac{1}{\rho_0}\nabla\tilde{p}-\nabla\cdot\boldsymbol{\tau}-f\mathbf{e}_z\times(\tilde{\mathbf{u}}+\mathbf{u}_s)+\mathbf{u}_s\times\tilde{\boldsymbol{\omega}} +\left(1-\frac{\tilde{\rho}}{\rho_0}\right)g\mathbf{e}_z+\left(1-\frac{\rho_d}{\rho_0}\right)\frac{\tilde{C}}{\rho_d}g\mathbf{e}_z \tag{1}$$

together with the incompressibility condition $\nabla\cdot\tilde{\mathbf{u}}=0$. Here a tilde denotes a variable resolved on the LES grid, $\mathbf{u}$ is the Eulerian velocity, $\mathbf{u}_s$ is the wave-induced Stokes drift velocity, $\boldsymbol{\omega}$ is the vorticity vector, and p is a modified pressure. In addition, $\boldsymbol{\tau}=(\widetilde{\mathbf{u}\mathbf{u}}-\tilde{\mathbf{u}}\tilde{\mathbf{u}})$ is the subgrid-scale (SGS) stress tensor, f is the Coriolis parameter, g is the gravitational acceleration, $\mathbf{e}_z$ is the unit vector in the vertical direction, ρ_0 is the reference density of sea water, ρ is the sea-water density, ρ_d is the density of oil, and C is the oil mass concentration field. The last three terms in equation (1) represent the vortex force due to wave-current interaction from the Craik-Leibovich equations [*Leibovich*, 1977, 1983], and two buoyancy forces induced by water density fluctuations and oil concentrations included in the momentum equation using the Boussinesq approximation.

We follow many previous studies on Langmuir turbulence using LES [e.g., *McWilliams et al*., 1997; *McWilliams and Sullivan*, 2000; *Kukulka et al*., 2009; *Yang et al*., 2014, 2015] and consider a swell propagating in deep-water condition. The corresponding Stokes drift velocity is specified as

$$\mathbf{u}_s(z)=\frac{\mathbf{k}}{k}U_s e^{2kz}, \tag{2}$$

where $\mathbf{k}=(k_x,k_y)$ is the wavenumber vector with magnitude k and $U_s=\sigma k a^2$ is the magnitude of Stokes drift velocity at the ocean surface [*McWilliams et al*., 1997]. Here a and $\sigma=\sqrt{gk}$ are the wave amplitude and angular frequency, respectively. Equation (2) is applicable for $z\leq 0$ with $z=0$ being the mean sea-surface level.

The oil field is described as a mass concentration $C(x,y,z,t)$ in continuous Eulerian form. This concentration field is evolved by a filtered advection-diffusion equation

$$\frac{\partial\tilde{C}}{\partial t}+\nabla\cdot\left[(\tilde{\mathbf{v}}+\mathbf{u_s})\tilde{C}\right]=-\nabla\cdot\boldsymbol{\pi}_C+Q_s\,, \tag{3}$$

where $\boldsymbol{\pi}_C=\left(\widetilde{\mathbf{u}C}-\tilde{\mathbf{u}}\tilde{C}\right)$ is the SGS oil concentration flux, Q_s is a source term, and

$$\tilde{\mathbf{v}}=\tilde{\mathbf{u}}+w_r\mathbf{e}_z+(R-1)\tau_d\frac{D\tilde{\mathbf{u}}}{Dt} \tag{4}$$

is the velocity of the oil concentration field [*Ferry and Balachandar*, 2001] with respect to the Stokes drift. Here $w_r=(\rho_0-\rho_d)gd^2/(18\mu_f)$ is the droplet rise velocity, d is the droplet diameter, μ_f is water viscosity, $R=3\rho_0/(2\rho_d+\rho_0)$ is the acceleration parameter, and $\tau_d=(\rho_d+\rho_0/2)d^2/(18\mu_f)$ is the droplet time scale.

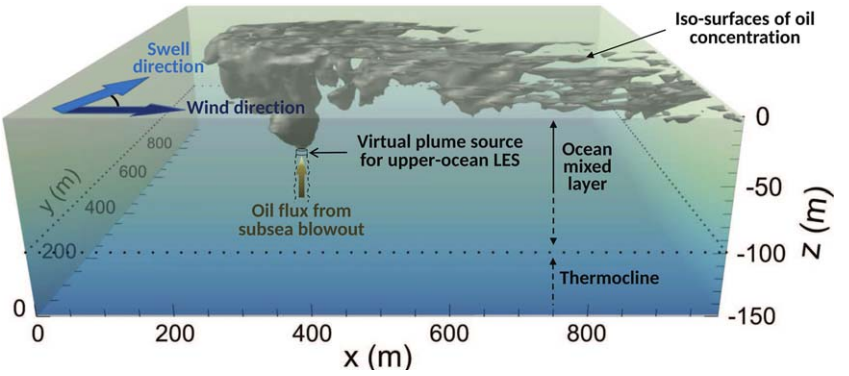

Figure 1. Sketch of LES simulation setup. A sample oil plume for the swell-wind angle $\alpha=45^\circ$ and oil droplet diameter $d=250\ \mu$m is shown for illustration. Note that a virtual oil source located within the thermocline is used to represent the oil plume arriving from a deepwater blowout.

An additional filtered advection-diffusion equation is solved for temperature θ, which is then related to seawater density via $\rho=\rho_0[1-\alpha(\theta-\theta_0)]$, where $\alpha=2\times10^{-4}\,\mathrm{K}^{-1}$ [*McWilliams et al*., 1997] is the thermal expansion rate and θ_0 is the reference temperature corresponding to the reference density ρ_0. The equation for θ is similar to equation (3), except that $\tilde{\mathbf{v}}$ is replaced by $\tilde{\mathbf{u}}$ and no source term is included.

To close the equation set, the SGS momentum flux is parameterized using the Lilly-Smagorinsky model [*Smagorinsky*, 1963; *Lilly*, 1967], and the Smagorinsky coefficient is determined dynamically during the simulation using the Lagrangian scale-dependent dynamic model [*Bou-Zeid et al*., 2005]. SGS heat and oil concentration fluxes $\boldsymbol{\pi}_\theta$ and $\boldsymbol{\pi}_C$ are then parameterized as $\boldsymbol{\pi}_\theta=-(\nu_\tau/\mathrm{Pr}_\tau)\nabla\tilde{\theta}$ and $\boldsymbol{\pi}_C=-(\nu_\tau/\mathrm{Sc}_\tau)\nabla\tilde{C}$ with constant SGS Prandtl and Schmidt numbers $\mathrm{Pr}_\tau=0.4$ and $\mathrm{Sc}_\tau=0.8$ [*Yang et al*., 2015].

The discretization for momentum and temperature equations combines a pseudo-spectral method on collocated grid in the horizontal directions and a second-order centered finite-difference scheme on staggered grid in the vertical direction. The boundary conditions for velocity, pressure, and temperature fields in the horizontal directions are periodic. The oil transport equation (3) is discretized following a finite-volume method, with the bounded third-order upwind interpolation scheme SMART [*Gaskell and Lau*, 1988] applied to the advection term. The coupling of the pseudo-spectral approach with the finite-volume discretization follows *Chamecki et al*. [2008]. The lateral boundary conditions for oil concentration are specified as zero-

Table 1. Simulation Parameters

Parameter (Unit)	Symbol	Value
Domain size (m)	$L_x\times L_y\times L_z$	1000×1000×300
Grid spacing (m)	$dx\times dy\times dz$	10×10×2
Grid points	$N_x\times N_y\times N_z$	100×100×150
Time step (s)	dt	0.1
Wind stress (N m^{-2})	τ_w	0.156
Friction velocity in water (cm s^{-1})	u_*	1.25
Wave amplitude (m)	a	2.38
Wave length (m)	λ	150
Stoke drift at surface (cm s^{-1})	U_s	15
Swell-wind angle (°)	α	0, ±30, ±45, ±60, ±90, ±135, 180
Coriolis frequency (s^{-1})	f	7×10^{-5}
Turbulent Langmuir number	La_t	0.29
Thermocline depth (m)	z_i	100
Droplet diameter (μm)	d	177, 250, 500
Droplet rise velocity (cm s^{-1})	w_r	0.27, 0.54, 2.17
Source node	$(i,j,k)_{src}$	(30, 80, 70)
Source location	$(x,y,z)_{src}$	(290, 790, −139)
Source mass flow rate (kg s^{-1})	Q_s	1.0
Reference sea-water density (km m^{-3})	ρ_0	1031.0
Viscosity of sea water (kg (ms)$^{-1}$)	μ_f	1.08×10^{-3}
Thermal expansion rate of water (K^{-1})	α_θ	2×10^{-4}
Oil density (kg m^{-3})	ρ_d	859.9

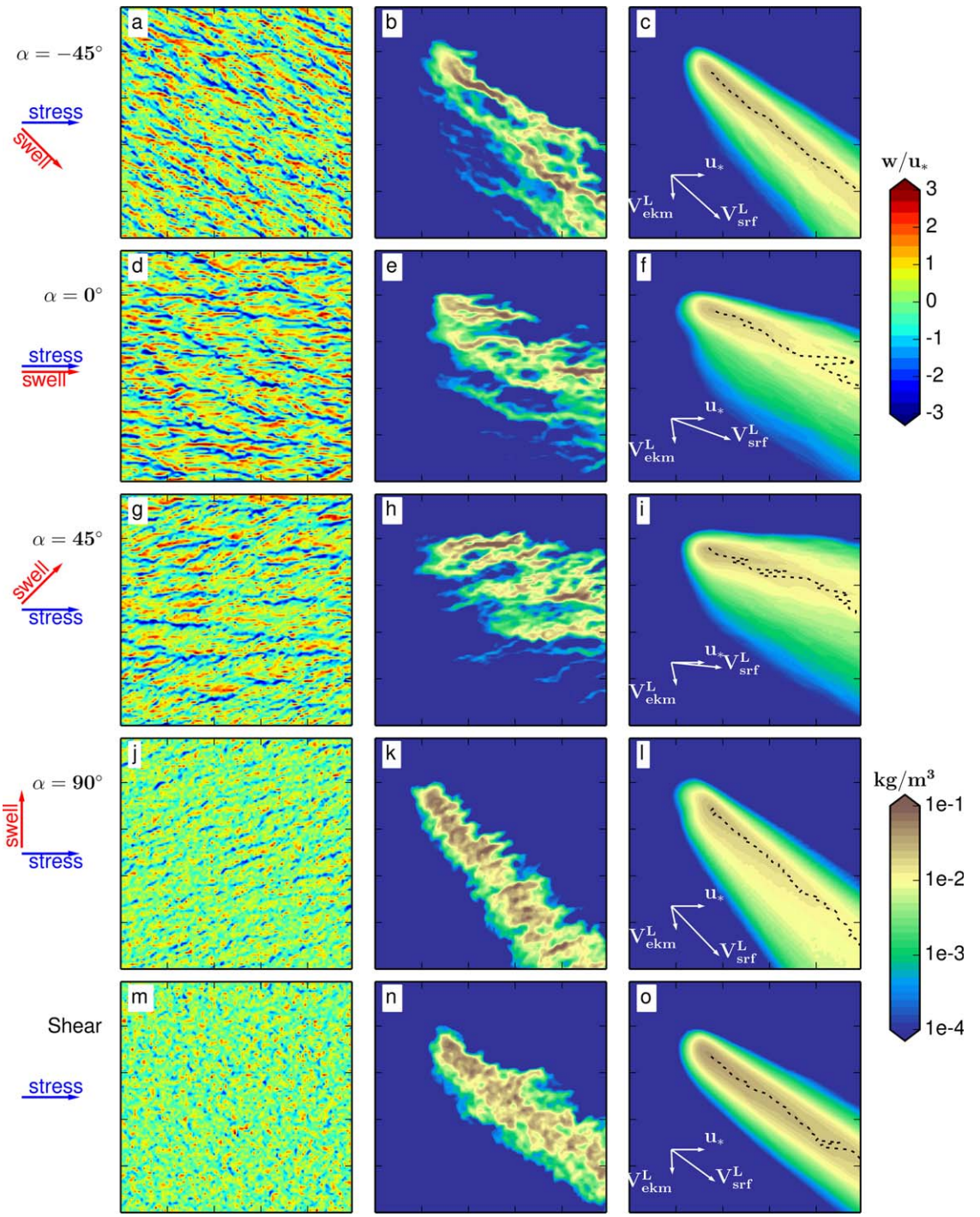

Figure 2. Vertical velocity fields at (a, d, g, j, m) $z = -6$ m depth, (b, e, h, k, n) instantaneous and (c, f, i, l, o) time-averaged surface oil concentration. The oil plumes shown here have oil droplet diameter $d = 500$ μm.

value for inflow and zero-gradient for outflow boundaries. Injection of oil into the domain is accomplished by means of a volume source as described in section 2.2. The time integrations for velocity, temperature, and oil concentration fields are carried on using second-order Adams-Bashforth scheme. A more detailed description of the model and the numerical discretization is given in *Yang et al.* [2015]. Comparisons between turbulence statistics obtained with the LES code used here and simulations by *Li et al.* [2005] and *McWilliams et al.* [1997] have been presented in *Yang et al.* [2014, 2015], respectively. The latter also included a comparison

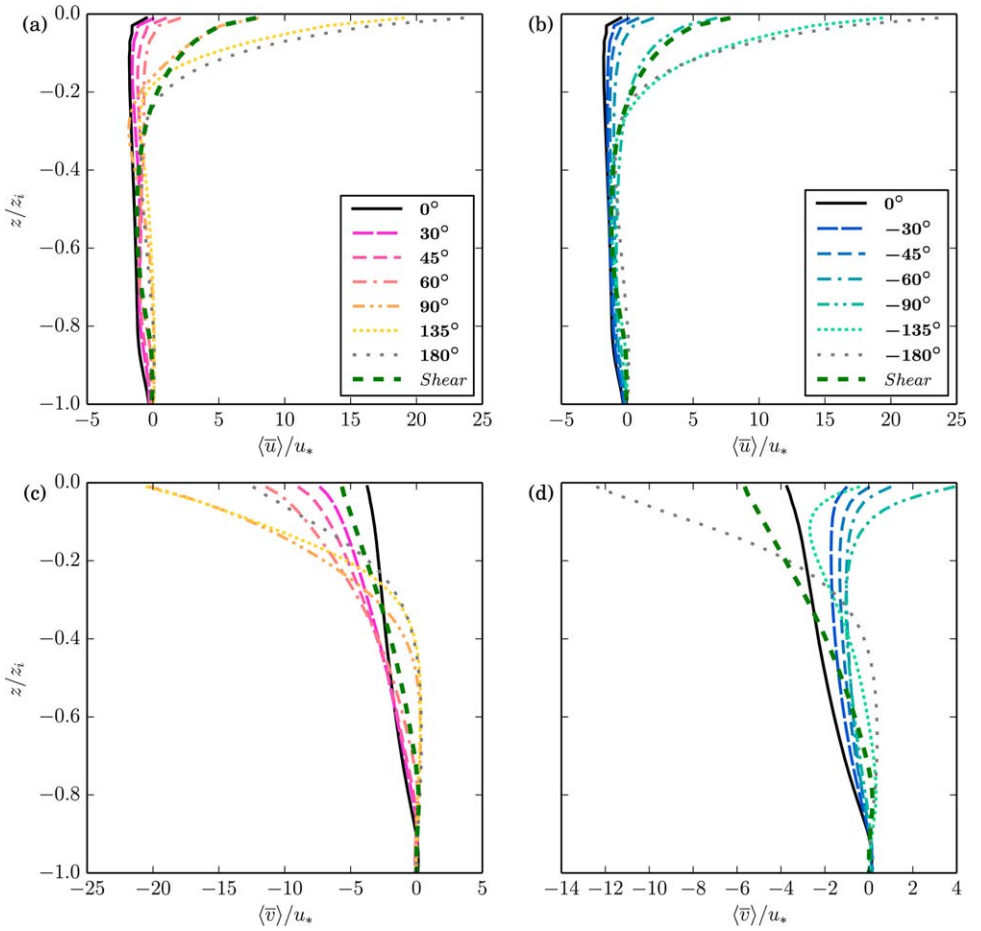

Figure 3. Vertical profiles of the time-averaged and horizontal-averaged velocity: (a, b) *u* component and (b, c) *v* component for (a, c) positive and (b, d) negative swell-wind angles. The no-swell shear turbulence case is labeled as "Shear."

with the vertical velocity variance profiles reported by *D'Asaro* [2001]. Qualitative comparisons between simulated oil plumes and pictures of oil slicks in the ocean were also shown in *Yang et al.* [2014]. Finally, a more quantitative comparison between results from simulations performed with the same numerical model and multiphase plumes in stably stratified environments from laboratory experiments has been presented by *Yang et al.* [2016].

2.2. Simulation Setup

The sketch of the simulation setup is shown in Figure 1 and the detailed simulation parameters are presented in Table 1. A constant wind stress $\tau_w = 0.156\,\mathrm{N\,m^{-2}}$ in the positive x direction is imposed on the ocean surface, corresponding to a wind of approximate 10 m s^{-1} at 10 m above the ocean surface or a friction velocity of $u_* = 0.0125\,\mathrm{m\ s^{-1}}$ in the ocean. A swell wave with wavelength of $\lambda = 150\,\mathrm{m}$ and amplitude of $a = 2.38\,\mathrm{m}$ is considered, yielding a surface Stokes drift with magnitude $U_s = 0.152\,\mathrm{m/s}$. The corresponding turbulent Langmuir number is $La_t = \sqrt{u_*/U_s} = 0.29$, which is a typical value from observations [*Belcher et al.*, 2012]. The overall experiment design is similar to the one used by *Van Roekel et al.* [2012], except that here we focus on the effects of swell on vertical eddy diffusivities and the transport of oil plumes. Note that effects of local wind waves are not included because the frequency of waves generated by local wind is typically 1 order of magnitude higher than that for the swell waves and their contribution to the total Stokes drift is very small [*Van Roekel et al.*, 2012]. A series of 12 simulations are performed with different imposed angles between the swell wave propagation direction and the wind stress (hereafter called swell-wind angle α), covering the entire range $-180^\circ \le \alpha \le 180^\circ$. Additionally, one simulation without any swell wave field (i.e., a no-swell turbulence case) is also considered for comparison. The Coriolis frequency is $f = 7\times10^{-5}\,\mathrm{s^{-1}}$, corresponding to a latitude of 28.7°N. The initial thermocline depth is $z_i = 100\,\mathrm{m}$ and the stably stratified

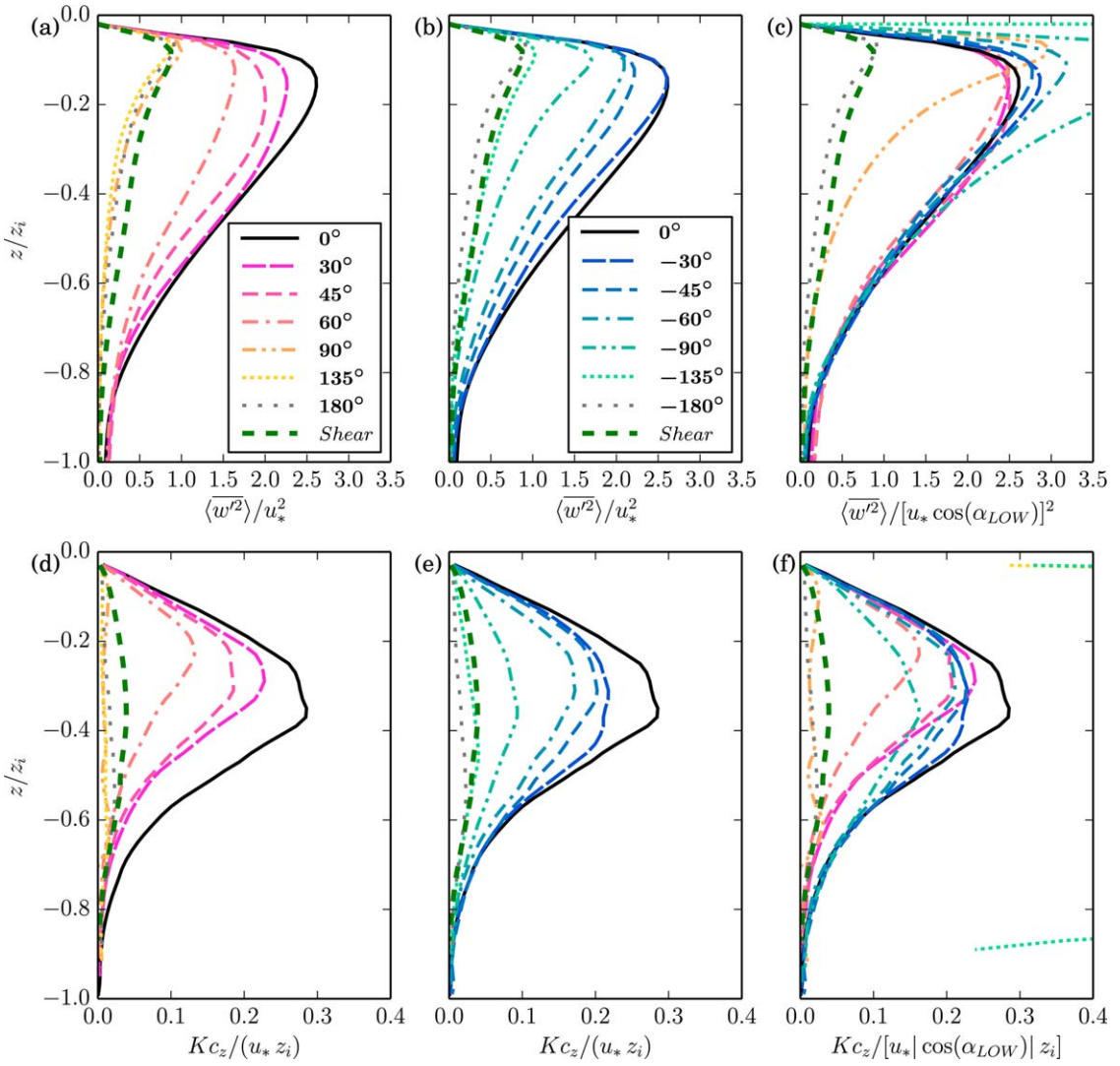

Figure 4. Vertical profiles of (a–c) vertical velocity variance and (d–f) vertical oil eddy diffusivity. Results for (a, d) positive and (b, e) negative swell-wind angles. Scaling based on *Van Roekel et al.* [2012] is also shown in Figures 4c and 4f.

layer below has an inversion strength $d\theta/dz = 0.01\,\mathrm{K\,m^{-1}}$. A weak outgoing heat flux from ocean surface, $Q = 15\,\mathrm{W\,m^{-2}}$, is imposed at the top boundary, which helps with the development of the OML. The analytical solution of a Stokes-Ekman layer in swell presented by *McWilliams et al.* [2014] is used to initialize the horizontal velocity components in the simulations. Because this solution is already a good approximation for the final equilibrium profiles and the wind forcing remains constant in time, no significant inertial oscillation is observed in any of the simulations.

The transport of oil plumes with different droplet sizes is investigated for each swell-wind angle. Three effective diameters, 177, 250, and 500 μm, are chosen, corresponding to rise velocities of 0.27, 0.54 and 2.16 $\mathrm{cm\,s^{-1}}$, respectively (see Table 1 for sea-water and oil properties used). Note that these velocities correspond to drift-to-buoyancy parameter $Db = U_s/w_r$ [*Yang et al.*, 2014] equal to 56, 28, and 6.9, suggesting that the resulting plumes have different responses to the downwelling motion in the Langmuir cells. In all the simulations, the oil is released from a localized source located below the thermocline at $(x, y, z) = (290, 790, -139)$ m with a releasing rate $Q_s = 1\,\mathrm{kg\,s^{-1}}$ [*Yang et al.*, 2014]. The simulation domain has a size of $(L_x, L_y, L_z) = (1000\,\mathrm{m}, 1000\,\mathrm{m}, 300\,\mathrm{m})$ and is discretized with $100 \times 100 \times 150$ grid points. The flow field is spun-up for a duration of 17.5 h, after which the oil release is initiated (the time step of the numerical integration is 0.1 s). Statistics are collected for another 17.5 h after the oil plumes has reached statistical steady state.

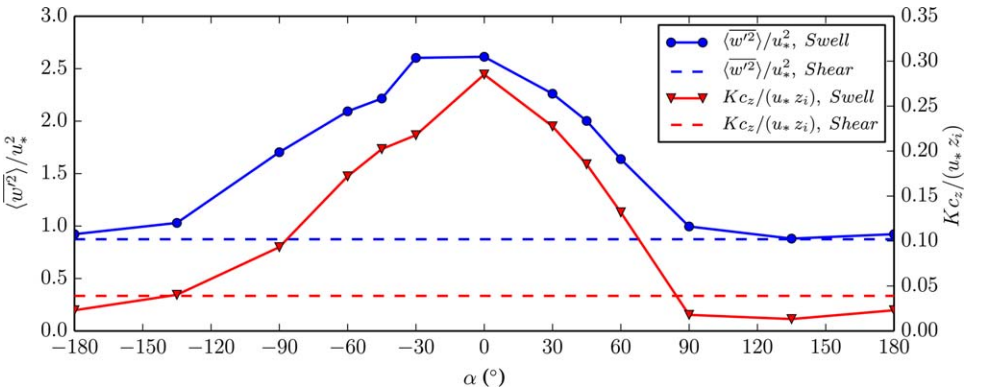

Figure 5. Maximum values of vertical velocity variance and eddy diffusivity as a function of swell-wind angle α.

3. LES Results

3.1. Statistics of Flow Field

Typically, the presence of Langmuir circulations can be visualized through the resulting narrow downwelling/upwelling zones in near-surface vertical velocity and the windrows on the ocean surface. These downwelling/upwelling patterns can be seen in Figure 2 for four selected swell-wind angle cases (left column), together with instantaneous surface oil plume patterns for the $d=500\ \mu$m oil droplets (middle column). As the swell direction varies, the orientation of Langmuir cells changes in the same direction of swell-wind angle α. As observed by *Van Roekel et al*. [2012], the Langmuir cell orientation is positioned between the wind stress and swell directions. The case with $\alpha=0^\circ$ is an exception, as the wind stress and swell are parallel and the Langmuir cell orientation is characterized by a negative angle due to the Coriolis effect. Interestingly, a strong asymmetry in cell orientation is observed between positive and negative swell-wind angles, as evidenced by the $\pm45^\circ$ cases. Meanwhile, only a weak signature of Langmuir cells exists when $\alpha=90^\circ$ and the magnitude of the vertical velocity fluctuation is similar to that for no-swell case.

Figure 3 shows vertical profiles of the averaged horizontal Eulerian velocity $(\langle\bar{u}\rangle, \langle\bar{v}\rangle)$ for various swell-wind angles α. Here angle brackets and overline denote horizontal and temporal averages, respectively. For $\alpha=0^\circ$, weak vertical shear is observed in the entire OML for both components of the mean velocity. In particular, the shear is much weaker than the one without swell effects due to the increased momentum

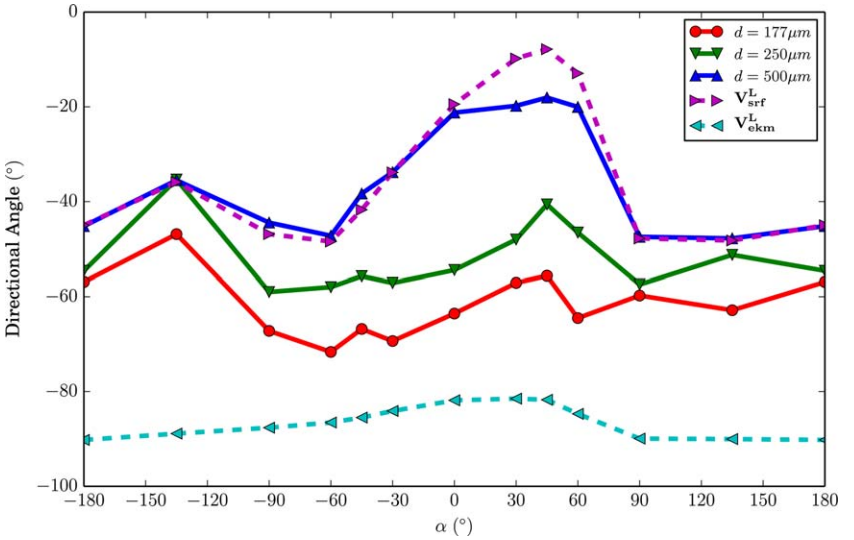

Figure 6. Mean plume direction as a function of swell-wind angle α. $\mathbf{V}^L_{srf}$ is the horizontal-averaged surface Lagrangian velocity, including the Eulerian velocity and Stokes drift velocity, while $\mathbf{V}^L_{ekm}$ is the horizontally as well as vertically averaged Lagrangian velocity (i.e., averaged also over the entire depth of the OML).

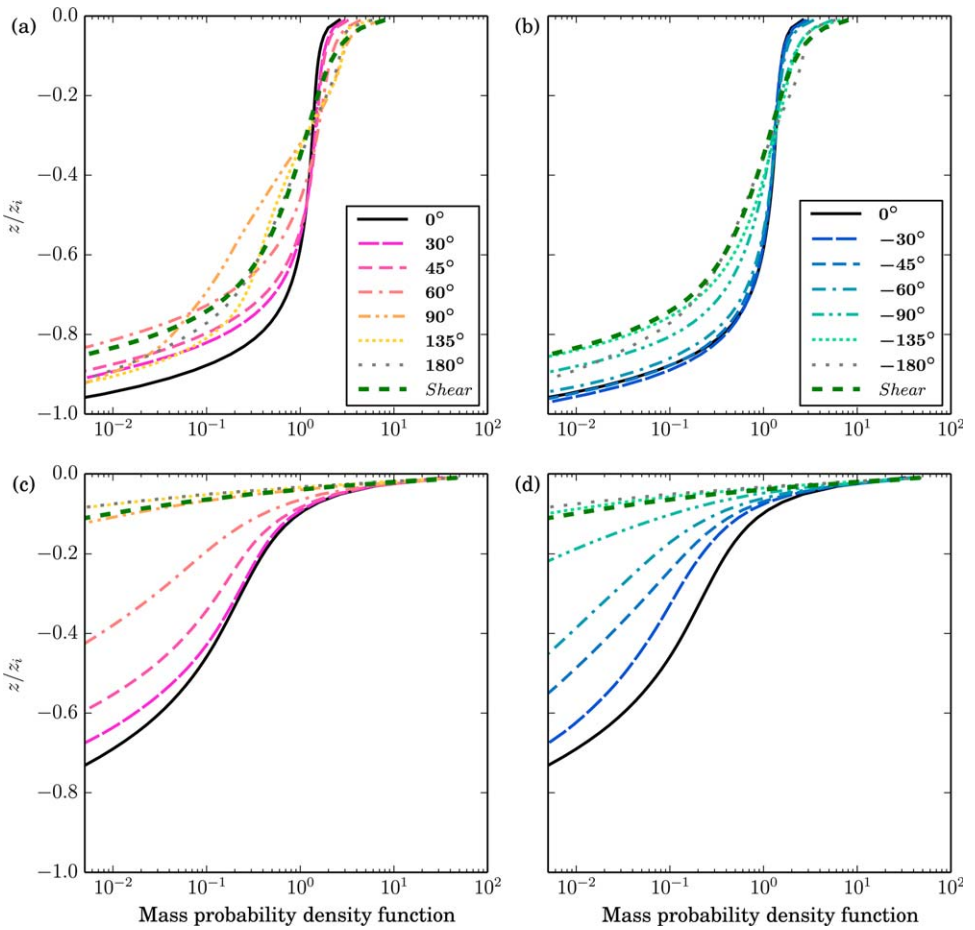

Figure 7. Vertical distribution of oil mass away from the vertically rising plume for oil droplet with (a, b) $d=177\ \mu$m and (c, d) $d=500\ \mu$m. Results are shown for (a, c) positive and (c, d) negative swell-wind angles.

transport induced by Langmuir circulations. As the magnitude of α increases, the shear in both velocity components increases in the upper part of the OML. Eventually, the vertical shear exceeds that for the no-swell case and the magnitudes of horizontal Eulerian velocity components in the upper part of the OML become much larger than that of $\alpha=0^\circ$. This result suggests that, for large angles, there is a reduction of the turbulent momentum flux in comparison to the no-swell case, which is contrary to the trend for small swell-wind angle regime.

The modulation of turbulence by Langmuir circulations is clearly seen on the vertical profiles of vertical velocity variance $\langle\overline{w'^2}\rangle$ (Figures 4a and 4b). The large effect of swell-wind angle on the magnitudes of $\langle\overline{w'^2}\rangle$ is in agreement with *Van Roekel et al.* [2012]. However, the asymmetry between positive and negative angles (e.g., note the large difference between the $\alpha=+90^\circ$ which is almost indistinguishable from the no-swell case, and $\alpha=-90^\circ$ with values of $\langle\overline{w'^2}\rangle$ almost twice as large) is at odds with the simulations from *McWilliams et al.* [2014], who found the vertical variance to be roughly symmetric about $\alpha=0^\circ$. A possible reason for the different trends is that in *McWilliams et al.* [2014], an additional wind-driven wave field is imposed in the simulations. The asymmetry is more evident in Figure 5, where the peak value of the vertical variance is shown as a function of the swell-wind angle. Figures 4 and 5 suggest that the vertical velocity variance is significantly modified by Langmuir cells for $-135^\circ < \alpha < 90^\circ$, and no large differences are observed between the no-swell case and the cases with large swell-wind angles (hereafter the cases inside/outside $-135^\circ < \alpha < 90^\circ$ range are referred to as small/large swell-wind angles).

To better scale the vertical velocity variance, we first start with the model proposed by *Van Roekel et al.* [2012] to estimate the orientation of Langmuir cells,

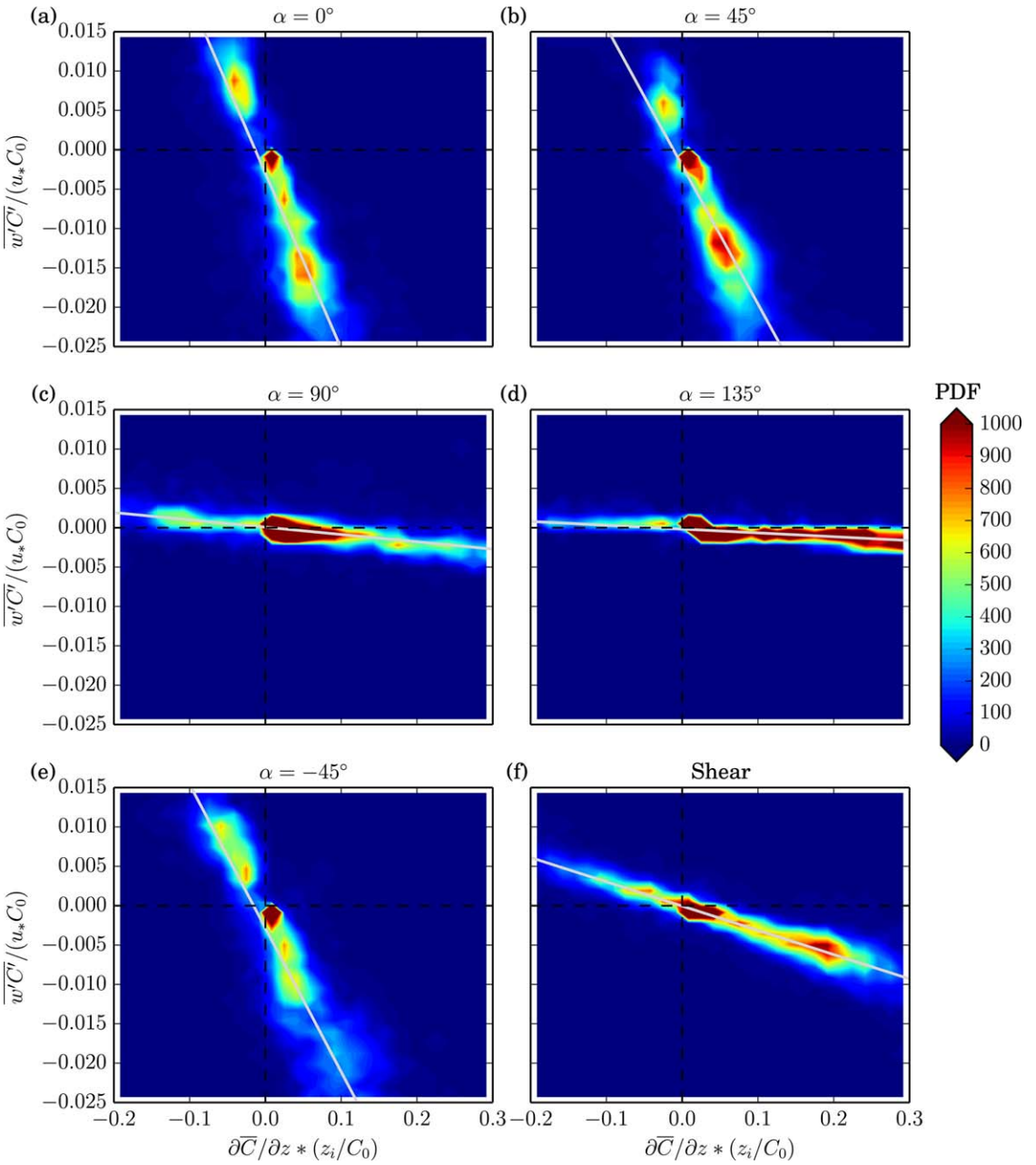

Figure 8. Joint probability density function (PDF) between normalized oil concentration gradient and turbulent oil concentration flux for $d=177\ \mu$m at the depth of $z/z_i=-0.2$. The concentration scale used for normalization is $C_0=Q_s/(u_*z_i^2)$. The gray lines represent the fitting based on equation (6), with the slope being the eddy diffusivity and the intercept the spatially averaged nonlocal flux.

$$\tan(\alpha_{LOW}) = \frac{\langle \partial_z v_s \rangle_{D_l}}{u_* \ln(D_l/z_1)/(\kappa|(D_l - z_1)|) + \langle \partial_z u_s \rangle_{D_l}}, \tag{5}$$

where $\langle\cdot\rangle_{D_l}$ represents a vertical average from the first grid point z_1 to the depth D_l (taken as twice the *e*-folding depth of the Stokes drift, which is about $0.24z_i$ in the present case). Here α_{LOW} is the angle between Langmuir cells and the mean wind direction estimated based on the assumption that the Eulerian mean velocity satisfies the law of the wall (note that *Teixeira* [2012] proposed a modified mean velocity profile that includes the effect of Langmuir number, but that model does not seem to improve the predictions for the low La_t condition used in these simulations). For the present simulations, we obtain $\alpha_{LOW}=0°, \pm18°, \pm27°, \pm36°, \pm55°, \pm90°, 180°$ for $\alpha=0°, \pm30°, \pm45°, \pm60°, \pm90°, \pm135°, 180°$, respectively. *Van Roekel et al.* [2012] argued that the friction velocity obtained from the component of the

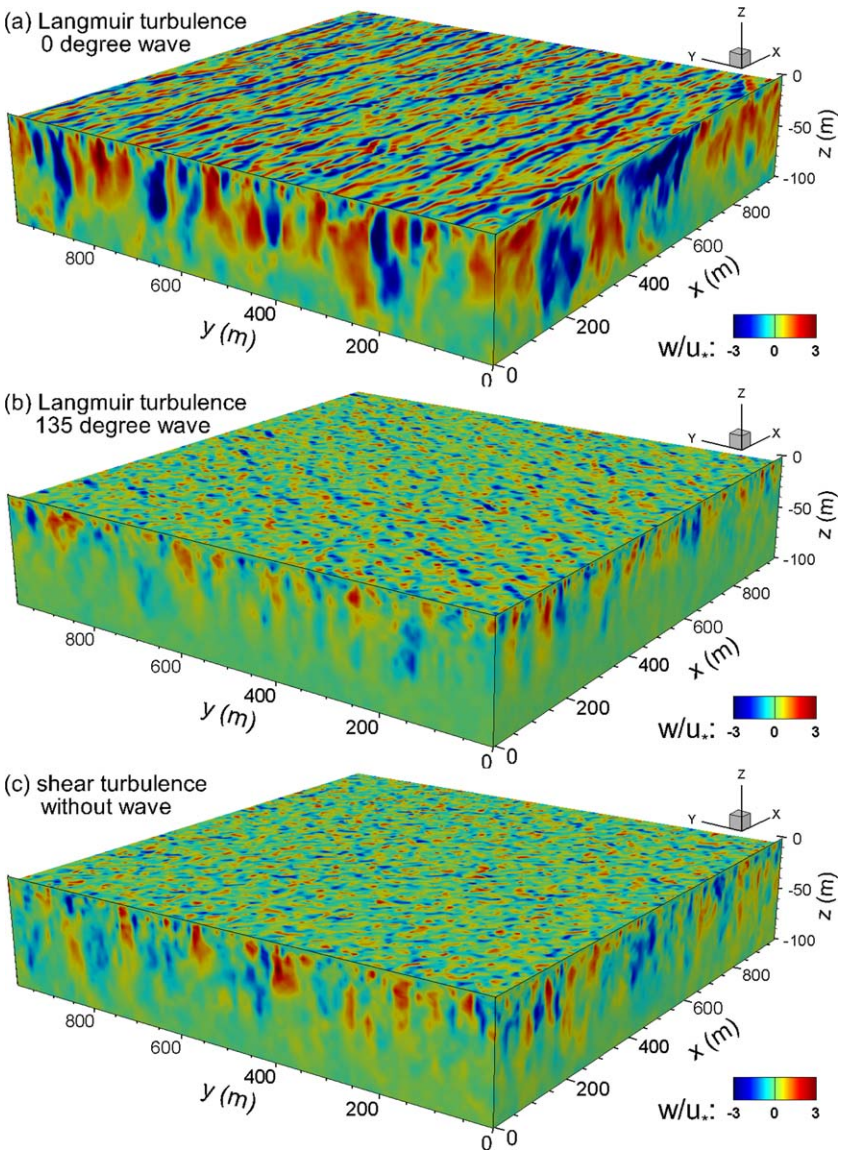

Figure 9. 3-D contours of instantaneous vertical velocity for various swell-wind angles equal to (a) 0°, (b) 135°, and (c) no-swell case.

surface shear stress aligned with the Langmuir cells (i.e., $u_*\cos(\alpha_{LOW})$) is the appropriate scale for the vertical velocity variance. Results presented in Figure 4c confirm this assertion, as the use of the modified friction velocity significantly reduces the spread between the different curves. The collapse is fairly good for the cases with significant Langmuir circulations ($-135^\circ < \alpha < 90^\circ$, small swell-wind angles) but not for the cases with weak Langmuir circulations.

3.2. Statistics of Oil Plumes

The middle and right columns in Figure 2 show the instantaneous and time-averaged surface oil plumes of large droplets (d=500 μm) for a few sample swell-wind angles. In the figure, $\mathbf{V}^L_{srf}$ denotes the mean Lagrangian velocity $\mathbf{u}_L$ at the ocean surface, where Lagrangian velocity is defined as $\mathbf{u}_L=\mathbf{u}_s+\mathbf{u}$ · In addition, $\mathbf{V}^L_{ekm}$ is the mean horizontal Lagrangian velocity in the OML (averaged within $-z_i \le z \le 0$), representing the mean Ekman transport velocity. The arrow labeled with u_* indicates the direction of the wind shear. The instantaneous oil surface plumes exhibit spatial patterns that resemble those of the vertical velocity. For these large oil droplets (i.e., small *Db* number), high-concentration regions in the shape of "fingers" coincide with the downwelling regions near the surface, as discussed by *Yang et al.* [2014]. Note that the mean transport direction of the surface time-averaged plume (denoted by the centerline in the right column of Figure 2) is

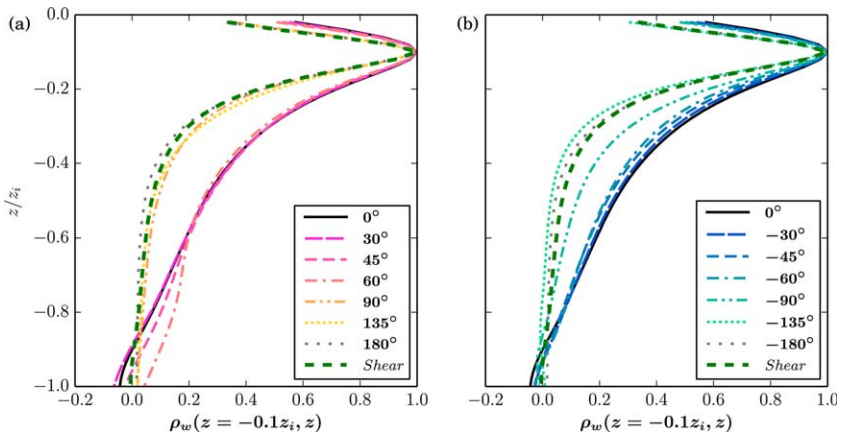

Figure 10. Autocorrelation between vertical velocity at $z=-0.1z_i$ and other depths z.

almost parallel to the surface Lagrangian velocity $\mathbf{V}^L_{srf}$. This is caused by the tendency of large oil droplets (with small *Db* numbers) to stay near the surface [*Yang et al*., 2014, 2015].

A more systematic study of the changes in the mean surface plume direction with droplet size and swell-wind angle is shown in Figure 6. Because the swell-induced Stokes drift velocity is large and has its maximum value at the surface, the direction of the mean surface Lagrangian velocity is more impacted by the swell-wind angle than the direction of the mean Ekman transport. The direction of the plumes of large droplets ($d=500\,\mu$m) with small *Db* tends to follow closely the direction of $\mathbf{V}^L_{srf}$. Meanwhile, the plumes of medium and small droplets ($d=250\,\mu$m and $d=177\,\mu$m, respectively) with larger *Db* tend to be more mixed

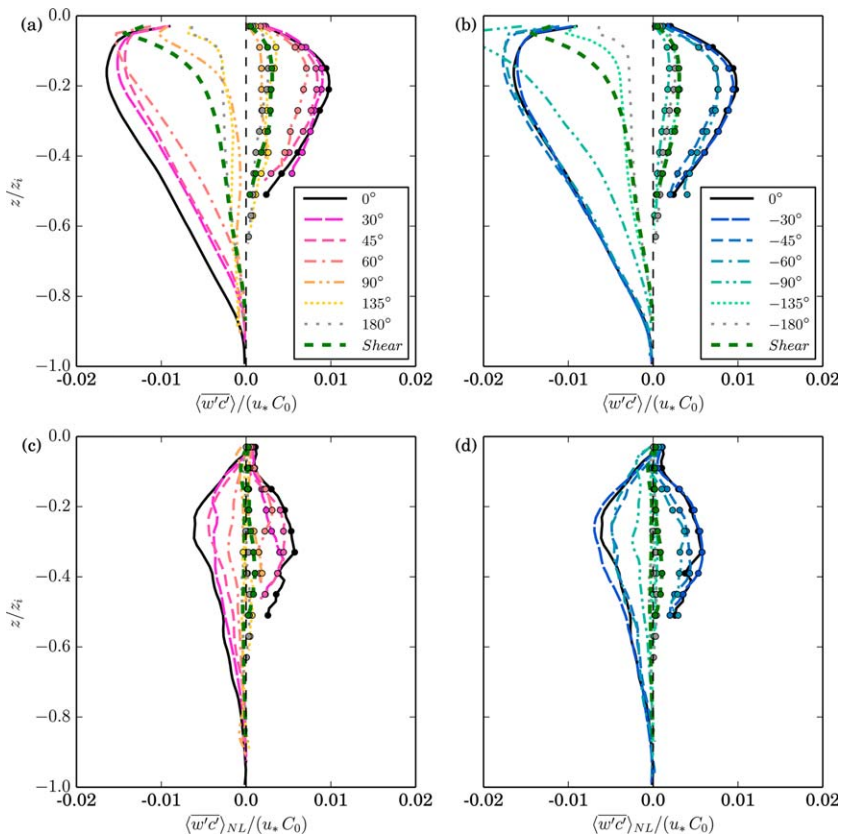

Figure 11. Spatially averaged (top row) total turbulent flux and (bottom row) nonlocal turbulent flux of oil concentration. The lines with/without circles represent results averaged over regions where the mean flux is negative/positive. The concentration scale used for normalization is $C_0=Q_s/(u_*z_i^2)$.

within the OML (Figure 7). Therefore, these plumes experience flow conditions within a deeper layer of the OML and the transport direction falls somewhere in between the directions of $\mathbf{V}^L_{srf}$ and $\mathbf{V}^L_{ekm}$.

Two additional details in Figure 6 are worthwhile mentioning. First, the direction of the large-droplet plume clearly deviates from $\mathbf{V}^L_{srf}$ for $0^\circ \leq \alpha \leq 60^\circ$ (Figure 6). This is caused by the enhancement of vertical mixing induced by the strong Langmuir circulations at small swell-wind angles. In these cases, even large droplets are constantly entrained into the OML by strong downwelling motions, producing slightly more mixed vertical oil concentration profiles (Figures 7c and 7d) that interact with the subsurface current. Notice that this phenomenon is not observed for small negative swell-wind angles. This is because for small negative angles, the Eulerian velocity is very small compared to the Stokes drift in the uppermost 10% of the OML (Figure 3). Therefore, the mean direction of the Lagrangian velocity has only a weak dependence on depth, and the increased vertical mixing does not impact the mean transport direction. Second, the directions of the medium-droplet and small-droplet plumes tend to approach $\mathbf{V}^L_{srf}$ for large swell-wind angles. This is caused by the suppression of vertical mixing for these large angle cases as discussed below.

The high sensitivity of the mean plume direction to the swell-wind angle motivates a more careful study of the vertical flux of oil concentration. Following common practice in studies of the convective boundary layer [e.g., *Holtslag and Moeng*, 1991] and Langmuir turbulence [e.g., *McWilliams and Sullivan*, 2000], the total turbulent flux is divided into a local component that is proportional to the mean concentration gradient (defining an eddy diffusivity for oil concentration Kc_z), and a nonlocal component that is independent of the local mean concentration gradient:

$$\overline{w'C'} = -Kc_z\,\partial_z\bar{C} + \overline{w'C'}_{NL}. \tag{6}$$

Here $\overline{w'C'}_{NL}$ is the nonlocal component of the total flux. Because the oil plumes in this study are highly inhomogeneous in all three spatial directions, the vertical eddy diffusivity Kc_z is estimated by a least squares fitting of the LES data at each depth z similar to the approach described by *Yang et al*. [2015]. In summary, with a scatterplot of $\overline{w'C'}$ against $\partial_z\bar{C}$ produced for each depth, the negative fitted slope is the value of Kc_z and the intercept is the spatially averaged nonlocal flux $\langle\overline{w'C'}_{NL}\rangle$ at that depth. Only points far from the location of the vertically rising plume (here assumed as the region outside a cylinder of radius 300 m centered at the source location) and with local concentration $\bar{C}$ larger than 2×10^{-6} kg m^{-3} are included in the calculation. In addition, a fit is only performed if more than 100 points are available for that depth.

Figure 8 shows the joint probability density function (PDF) of normalized $\overline{w'C'}$ and $\partial_z\bar{C}$ as well the corresponding fitting line for the smallest oil droplet size (d=177 μm) at z/z_i=−0.2 for several swell-wind angles. As expected, the PDF has a peak in the fourth quadrant ($\partial_z\bar{C} > 0$ and $\overline{w'C'} < 0$), corresponding to higher concentrations near the surface and downward turbulent fluxes. In most cases, a nonnegligible portion of the PDF is in the second quadrant ($\partial_z\bar{C} < 0$ and $\overline{w'C'} > 0$), and these points tend to form a well-defined secondary peak in cases with strong Langmuir cells (small swell-wind angles in Figures 8a, 8b, and 8e). Note that the points in the second quadrant are not just turbulent fluctuations, as each point used in the PDF represents a time average at a fixed location. Therefore, in some regions of the domain, the mean flux is directed upward. This is because Langmuir turbulence is strong enough to transport oil droplets downward by downwelling events (Figure 7). Due to changes in the mean horizontal velocity with depth associated with the Ekman spiral, these oil droplets can be advected in a lateral direction relative to the surface plume. This lateral transport creates a negative vertical gradient of oil concentration ($\partial_z\bar{C} < 0$) and positive turbulent flux of oil ($\overline{w'C'} > 0$) at the lateral (in the clockwise direction) edge of plume.

Eddy diffusivity profiles $Kc_z(z)$ for the smallest oil droplet size (d=177 μm) are shown in Figures 4c and 4d (profiles for larger droplets are similar but have more noise due to the smaller number of samples at larger depths). The profiles of $Kc_z(z)$ have similar trends as those for the vertical velocity variance (Figures 4a and 4b), in the sense that large decreases in eddy diffusivity are observed for increasing misalignment. However, differently from the vertical velocity variance, the eddy diffusivity for large swell-wind angles decreases to levels much lower than that of the no-swell case. This trend becomes very clear when the maximum values for each profile of $\langle\overline{w'^2}\rangle$ and Kc_z are displayed as a function of α in Figure 5. Note how the peak of Kc_z reduces to levels much lower than the one for the no-swell case (the same is not true for the vertical velocity variance).

Similar to the variance of vertical velocity, the eddy diffusivity Kc_z scales well with the modified friction velocity $u_* \cos(\alpha_{LOW})$. Results from LES (Figure 4f) show that this scaling captures part of the variability in Kc_z for the small angle cases, suggesting that the modified velocity can even be used as a simple first-order model for the eddy diffusivity modulations in swell conditions. However, the further decreases in eddy diffusivity for large swell-wind angles are not captured and reflect a more profound modification of oil transport mechanisms.

The difference in the behaviors of $\langle \overline{w'^2} \rangle$ and Kc_z for large swell-wind angles can be understood in light of the modification of vertical eddy scales by wave-current interactions. Figure 9 shows cuts of the three-dimensional instantaneous vertical velocity field for three simulations. For the no-swell case (Figure 9c), turbulence is produced by the wind shear and the largest eddies extend almost to the bottom of the OML. These large eddies entrain oil droplets from the surface and transport them throughout most of the OML, mixing the profile and yielding significant vertical eddy diffusivities. For the case with $\alpha = 0^\circ$ (Figure 9a), there are strong Langmuir circulations penetrating the entire OML. The vertical velocity variance is much stronger than in the no-swell case, transporting oil downward more efficiently and enhancing the vertical eddy diffusivity. For $\alpha = 135^\circ$ (Figure 9b), although the profile of vertical velocity variance is similar to the no-swell case (Figure 4a), the vertical extent of the eddies is reduced (Figures 9b and 9c). This scale suppression is caused by the stabilizing effect of the vortex force when wave and current are in opposite directions [*Leibovich*, 1983], which is analogous to a statically stable density stratification. This reduction of the depth reached by surface eddies contributes to the decrease in eddy diffusivity when compared to the no-swell case.

This change in vertical penetration of large-scale eddies can be quantified by the autocorrelation function. Here the autocorrelation between the vertical velocity at $z = -0.1 z_i$ (which corresponds approximately to the peak in vertical velocity variance) and other depths z within the OML is employed (Figure 10). The presence of Langmuir circulations significantly increases the correlations for small swell-wind angles. For large angles, the effects are opposite and a significant reduction in correlation is observed. This result, together with the changes in the vertical velocity variance, explains most of the behavior of the vertical eddy diffusivity Kc_z.

Because Langmuir circulations are highly organized vortices that induce strong downwelling motion, the nonlocal transport of oil can be important when compared to the local component of the flux. As discussed above, the fitting approach illustrated in Figure 8 yields the horizontally averaged nonlocal flux at a given depth in the far field. However, the combined effects of Langmuir turbulence and Ekman transport lead to a plume geometry in which both local and nonlocal fluxes at a fixed depth change sign within the plume. The spatial averaging over regions of positive and negative fluxes results in small values of $\langle \overline{w'C'}_{NL} \rangle$ that do not reflect the importance of this process. To avoid this problem, the nonlocal flux is estimated as the intercept obtained by fitting $\overline{w'C'}$ with $\partial_z \bar{C}$ in quadrants two and four separately (this is equivalent to using the sign of the total flux as a proxy for the sign of the nonlocal flux). The resulting profiles are shown in Figure 11, together with the averaged total fluxes over the same regions. As expected from the profiles of oil concentration shown in Figure 7, the total fluxes decrease with increasing swell-wind angle. Similarly, the nonlocal fluxes also decrease. The most interesting feature of Figure 11 is the contribution of the nonlocal flux to the total flux, which can be larger than about 30% for cases with small swell-wind angles (i.e., strong Langmuir circulations) and become negligible for cases with no swell or with large swell-wind angles. Because these are still horizontal averages, it is possible that in some specific locations the contribution is even larger. Note that current closures used in regional ocean circulation models (e.g., the K-profile parameterization) [*Large et al.*, 1994] include a parameterization of the nonlocal fluxes for temperature or density, but it is based on surface fluxes and would not be applicable to oil plumes in which no surface flux is present.

4. Conclusions

In this study, the effects of the misalignment between the directions of the wind forcing and the swell propagation on the upper ocean transport of oil from a deepwater blowout were studied using a high-fidelity LES model. In particular, the swell-wind angle has a profound effect on the turbulence structure and, consequently, oil transport within the OML. Simulation results showed that for small swell-wind angles, the

vertical velocity variance and the penetration depth of the large eddies are significantly enhanced when compared to the no-swell case. Their combined effects lead to large vertical eddy diffusivities and strong nonlocal fluxes. Consequently, surface oil plumes become more mixed in the vertical direction. Conversely, for large swell-wind angles, there is a small suppression of the vertical velocity variance and a large reduction in the penetration depth of the large eddies. This reduction in vertical eddy size is caused by the stabilizing effects of the vortex force when the swell-wind angle is large, and it is the main cause for a drastic reduction in vertical eddy diffusivities and nonlocal fluxes observed here. Thus, the presence of swell leads to oil plumes that can be shallower or deeper than those observed for the no-swell case, depending on the swell-wind angle. Plume depth determines the layers of the OML that contribute the most to the mean oil transport. Thus, due to the strong directional shear of the mean flow in OML, plume depth effectively determines the mean plume direction.

It is important to be noted that, for a given swell-wind alignment, droplet size also plays an important role in determining plume depth, as described by *Yang et al*. [2015] and illustrated in Figure 6. For oil plumes with large droplets, which are likely more representative of oil slicks in the absence of dispersants, and under the conditions studied here, the changes in the swell-wind alignment alone can shift the mean transport direction by 25°. Similarly, a change in droplet size caused by the surface application of dispersants would significantly reduce droplet size and change the response of the oil plume to the OML dynamics, shifting the mean plume direction. Inclusion of these effects in regional models used to predict oil fate requires a parameterization to represent the effects of Langmuir turbulence and swell-wind alignment on the eddy diffusivity and a new closure model capable of capturing the spatial variability of the nonlocal flux.

Acknowledgments
This research was made possible by a grant from The Gulf of Mexico Research Initiative. Data are publicly available through the Gulf of Mexico Research Initiative Information & Data Cooperative (GRIIDC) at https://data.gulfresearchinitiative.org/data/R2.x224.000:0005/ (doi:10.7266/N76M34T1).

References

Belcher, S. E., et al. (2012), A global perspective on Langmuir turbulence in the ocean surface boundary layer, *Geophys. Res. Lett.*, *39*, L18605, doi:10.1029/2012GL052932.

Bou-Zeid, E., C. Meneveau, and M. Parlange (2005), A scale-dependent Lagrangian dynamic model for large eddy simulation of complex turbulent flows, *Phys. Fluids*, *17*(2), 025105, doi:10.1063/1.1839152.

Chamecki, M., C. Meneveau, and M. Parlange (2008), A hybrid spectral/finite-volume algorithm for large-eddy simulation of scalars in the atmospheric boundary layer, *Boundary Layer Meteorol.*, *128*(3), 473–484, doi:10.1007/s10546-008-9302-1.

D'Asaro, E. A. (2001), Turbulent vertical kinetic energy in the ocean mixed layer, *J. Phys. Oceanogr.*, *31*(12), 3530–3537.

Ferry, J., and S. Balachandar (2001), A fast Eulerian method for disperse two-phase flow, *Int. J. Multiphase Flow*, *27*(7), 1199–1226, doi:10.1016/S0301-9322(00)00069-0.

Gaskell, P. H., and A. K. C. Lau (1988), Curvature-compensated convective transport: Smart, a new boundedness-preserving transport algorithm, *Int. J. Numer. Methods Fluids*, *8*(6), 617–641, doi:10.1002/fld.1650080602.

Hanley, K. E., S. E. Belcher, and P. P. Sullivan (2010), A global climatology of wind-wave interaction, *J. Phys. Oceanogr.*, *40*(6), 1263–1282.

Holtslag, A., and C.-H. Moeng (1991), Eddy diffusivity and countergradient transport in the convective atmospheric boundary layer, *J. Atmos. Sci.*, *48*(14), 1690–1698.

Huntley, H. S., B. L. Lipphardt, and A. D. Kirwan (2013), *Surface Drift Predictions of the Deepwater Horizon Spill: The Lagrangian Perspective*, pp. 179–195, AGU, Washington, D. C., doi:10.1029/2011GM001097.

Kukulka, T., A. J. Plueddemann, J. H. Trowbridge, and P. P. Sullivan (2009), Significance of Langmuir circulation in upper ocean mixing: Comparison of observations and simulations, *Geophys. Res. Lett.*, *36*, L10603, doi:10.1029/2009GL037620.

Langmuir, I. (1938), Surface motion of water induced by wind, *Science*, *87*(2250), 119–123.

Large, W. G., J. C. McWilliams, and S. C. Doney (1994), Oceanic vertical mixing: A review and a model with a nonlocal boundary layer parameterization, *Rev. Geophys.*, *32*(4), 363–403, doi:10.1029/94RG01872.

Le Henaff, M., V. H. Kourafalou, C. B. Paris, J. Helgers, Z. M. Aman, P. J. Hogan, and A. Srinivasan (2012), Surface evolution of the deepwater horizon oil spill patch: Combined effects of circulation and wind-induced drift, *Environ. Sci. Technol.*, *46*(13), 7267–7273, doi:10.1021/es301570w.

Leibovich, S. (1977), On the evolution of the system of wind drift currents and Langmuir circulations in the ocean. Part 1. Theory and averaged current, *J. Fluid Mech.*, *79*, 715–743, doi:10.1017/S002211207700041X.

Leibovich, S. (1983), The form and dynamics of Langmuir circulations, *Ann. Rev. Fluid Mech.*, *15*(1), 391–427.

Li, M., C. Garrett, and E. Skyllingstad (2005), A regime diagram for classifying turbulent large eddies in the upper ocean, *Deep Sea Res., Part I*, *52*(2), 259–278.

Lilly, D. K. (1967), The representation of small scale turbulence in numerical simulation experiments, in *IBM Scientific Computing Symposium on Environmental Sciences*, pp. 195–210, Yorktown Heights, N. Y.

McWilliams, J. C., and P. P. Sullivan (2000), Vertical mixing by Langmuir circulations, *Spill Sci. Technol. Bull.*, *6*(34), 225–237, doi:10.1016/S1353-2561(01)00041-X.

McWilliams, J. C., P. P. Sullivan, and C.-h. Moeng (1997), Langmuir turbulence in the ocean, *J. Fluid Mech.*, *334*, 1–30, doi:10.1017/S0022112096004375.

McWilliams, J. C., E. Huckle, J. Liang, and P. P. Sullivan (2014), Langmuir turbulence in swell, *J. Phys. Oceanogr.*, *44*(3), 870–890.

Noh, Y., H. S. Min, and S. Raasch (2004), Large eddy simulation of the ocean mixed layer: The effects of wave breaking and Langmuir circulation, *J. Phys. Oceanogr.*, *34*(4), 720–735.

Phillips, O. M. (1966), *The Dynamic of Upper Ocean*, Cambridge Univ. Press, Cambridge, London, U. K.

Scotti, A. (2010), Large eddy simulation in the ocean, *Int. J. Comput. Fluid Dyn.*, *24*(10), 393–406, doi:10.1080/10618562.2010.522527.

Skyllingstad, E. D. (2000), Scales of Langmuir circulation generated using a large-eddy simulation model, *Spill Sci. Technol. Bull.*, *6*(34), 239–246, doi:10.1016/S1353-2561(01)00042-1.

Skyllingstad, E. D., and D. W. Denbo (1995), An ocean large-eddy simulation of Langmuir circulations and convection in the surface mixed layer, *J. Geophys. Res.*, *100*(C5), 8501–8522.

Smagorinsky, J. (1963), General circulation experiments with the primitive equations: I. the basic experiment, *Mon. Weather Rev.*, *91*(3), 99–164.

Sullivan, P. P., and J. C. McWilliams (2010), Dynamics of winds and currents coupled to surface waves, *Ann. Rev. Fluid Mech.*, *42*, 19–42.

Teixeira, M. A. (2012), The influence of Langmuir turbulence on the scaling for the dissipation rate in the oceanic boundary layer, *J. Geophys. Res.*, *117*, C05015, doi:10.1029/2011JC007235.

Van Roekel, L., B. Fox-Kemper, P. Sullivan, P. Hamlington, and S. Haney (2012), The form and orientation of Langmuir cells for misaligned winds and waves, *J. Geophys. Res.*, *117*, C05001, doi:10.1029/2011JC007516.

Yang, D., M. Chamecki, and C. Meneveau (2014), Inhibition of oil plume dilution in Langmuir ocean circulation, *Geophys. Res. Lett.*, *41*, 1632–1638, doi:10.1002/2014GL059284.

Yang, D., B. Chen, M. Chamecki, and C. Meneveau (2015), Oil plumes and dispersion in Langmuir, upper-ocean turbulence: Large-eddy simulations and K-profile parameterization, *J. Geophys. Res. Oceans*, *120*, 4729–4759, doi:10.1002/2014JC010542.

Yang, D., B. Chen, S. A. Socolofsky, M. Chamecki, and C. Meneveau (2016), Large-eddy simulation and parameterization of buoyant plume dynamics in stratified flow, *J. Fluid Mech.*, *794*, 798–833.